

Coupling Alkaline Conversion Zn Anode with Acidic Proton-insertion MoO₃ Cathode for High-voltage Aqueous Rechargeable Hybrid Battery

Pingwei Cai

Fujian Institute of Research on the Structure of Matter, Chinese Academy of Sciences

<https://orcid.org/0000-0001-7958-1781>

Yichun Ding

Fujian Institute of Research on the Structure of Matter

Yangjie Liu

College of Materials Science and Engineering, Fuzhou University

Zhenhai Wen (✉ wen@fjirsm.ac.cn)

Fujian Institute of Research on the Structure of Matter

Article

Keywords: alkali-acid Zn-MoO₃, hybrid battery, H⁺, OH⁻

Posted Date: July 16th, 2020

DOI: <https://doi.org/10.21203/rs.3.rs-39946/v1>

License:   This work is licensed under a Creative Commons Attribution 4.0 International License.

[Read Full License](#)

Abstract

Hydrogen ions (H^+) and hydroxide ions (OH^-) are regarded as ideal charge carriers for rechargeable batteries thanks to their small size, high ion mobility, low cost, and wide flexibility compared to the metal ions. However, the implementation of storage of both H^+ and OH^- in one electrochemical energy device face grand challenge due to incompatibility between H^+ and OH^- . Herein, we report an alkali-acid Zn-MoO₃ hybrid battery that employ H^+ and OH^- as charge carriers of cathode and anode, respectively, in which the insertion/deinsertion of H^+ take place on layer structured MoO₃ cathode in acid while OH^- are involved in alkaline conversion Zn anode, which offers a promising route to well address the incompatible issues of H^+ and OH^- in one electrolyte. The as-built hybrid battery can deliver a high open-circuit voltage of 1.85 V, a high rate capability, a high capacity of 158 mAh g⁻¹ at a current density of 5 A g⁻¹, and excellent capacity retention of above 90% over 200 cycles. This work sheds light on the development of aqueous energy devices with high voltage and energy density through materials engineering and device optimization.

Introduction

Electrochemical energy storage and conversion systems play a crucial role in the development of renewable energy for a sustainable future.^{1,2,3} Among these systems, aqueous-based batteries that employing metal ions as charge carriers, such as Zn-ion battery,^{4,5,6} have drawn worldwide attentions due to the advantages of environmental benignity, high safety, high efficiency, and fast kinetics. Whilst nonmetal ions battery,^{7,8,9,10} such as hydrogen ions (H^+), hydroxide ions (OH^-), NO_3^- , and NH_4^+ , receive rare research interest it deserved because they are actually ideal charge carriers for rechargeable batteries, thanks to their small size, high ion mobility, low cost, and wide flexibility compared to the metal ions.^{11,12} Moreover, it remains a grand challenge for the development of rechargeable battery with dual-nonmetal ions as charge carriers of both anode and cathode.^{13,14,15} In this regard, it is of great significance to explore the feasibility of developing aqueous batteries with dual-nonmetal ions as charge carriers and to clarify the associated electrochemical mechanism. Of various nonmetal ions, H^+ and OH^- are the ideal candidates as charge carriers for the dual-nonmetal ions battery with hydrogen insertion/deinsertion in cathode and OH^- involved in conversion anode (e.g., Zn, Al, Mg anode), respectively. To this end, at least two critical issues should be addressed. On one hand, an essential prerequisite for implementing such hybrid electrochemical device is to explore suitable cathode materials with capability for reversible H^+ insertion/deinsertion. On the other hand, it is a daunting challenge to integrate H^+ and OH^- in one electrochemical system because these two ions would react quickly once mixed.

Orthorhombic α -MoO₃ is one of the promising materials for H^+ storage,^{16,17} which is appropriate for the insertion/deinsertion of H^+ due to its layered structure.^{18,19,20} However, the poor conductivity and the limited electrochemical activity of α -MoO₃ greatly restrict its electrochemical H^+ storage capability and

thus behave low specific capacity and fast decay.^{21, 22} Accordingly, efforts have been made to improve the conductivity of α - MoO_3 , typically by coating of conductive polymers on the surface of MoO_3 ,^{23, 24, 25} such as polyaniline (PANI), polypyrrole (Ppy), owing to their merits of good stability, low cost, and good conductivity, which is beneficial to facilitate electrons transfer and to expedite ions exchange, in this manner can the associated performance be improved to a certain extent, there is great space for further improvement yet.^{26, 27}

The bottleneck for such electrochemical device with non-metal ions storage is the thermal stability windows of 1.23 V, which greatly limits the energy density that is directly related to the working voltage according to the equation ($E = C_{\text{sp}} * V$).^{28, 29} Hybrid electrochemical devices by coupling acidic cathode with alkaline anode were reportedly to be capable of broadening the voltage window of aqueous battery,^{30, 31, 32, 33, 34, 35} which inspire us to accomplish the idea to develop dual-nonmetal ions H^+/OH^- battery. We herein report a surface engineering and defect manufacturing route for fabrication of vacancy-riched MoO_3 porous nanobelt ($v\text{-MoO}_3$ PNB), which hold abundant oxygen defects and enlarged surface area, leading to more exposed active sites and improved electrical conductivity and allowing faster kinetics for H^+ insertion/deinsertion. We demonstrate the $v\text{-MoO}_3$ PNB exhibits a specific capacity of 210 mAh g^{-1} at 5 A g^{-1} and a high rate performance. Furthermore, we put forward an alkali-acid Zn- MoO_3 hybrid battery by coupling alkaline Zn anode with acidic $v\text{-MoO}_3$ PNB cathode that can liberate impressively high voltage and energy density.

Results

The synthesis process of $v\text{-MoO}_3$ PNB is schematically illustrated (Fig. S1, supporting information), which start a modified hydrothermal method reported previously for the synthesis of MoO_3 nanobelt (MoO_3 NB),¹⁸ which was then treated by FeCl_3 solution.³⁶ The $v\text{-MoO}_3$ PNB was finally obtained by partially reduction upon thermally annealing with $\text{NaH}_2\text{PO}_2 \cdot \text{H}_2\text{O}$ as reductant at $250 \text{ }^\circ\text{C}$ for 1 h according to the following reactions:



The as-prepared $v\text{-MoO}_3$ PNB, similar to that of MoO_3 NB, shows typical x-ray diffraction (XRD) patterns of orthorhombic MoO_3 phase (JCPDS#35-0609) with three dominant peaks that can be well indexed to (020), (040), and (060) crystalline facets. (Fig. 1a). Notably, one can obviously observe negative shifts of peak (020), (040), and (060) for $v\text{-MoO}_3$ PNB relative to those of MoO_3 NB (Fig. S2, supporting information), implying the increase of lattice spacing in $v\text{-MoO}_3$ PNB arising from the introduction of oxygen vacancies.^{37, 38} Fig. 1b-c show the typical scanning electron microscopy (SEM) images of MoO_3 NB, displaying a smooth nanobelt morphology with an average width of 240 nm and lengths about 5-10

μm (Fig. S3, supporting information), while the $v\text{-MoO}_3$ PNB show an eminently rough surface due to the etching treatment of FeCl_3 solution (Fig. 1d-e) with well maintaining nanobelt structure (Fig. S4, supporting information). It is noted that the color changes from the grey-white of MoO_3 NB to the blue of the $v\text{-MoO}_3$ PNB (Fig. S5, supporting information), further confirming inducing the surface defects of oxygen vacancies. The transmission electron microscopy (TEM) image convinces the existence of the porous structure in $v\text{-MoO}_3$ PNB (Fig. 1f). High-resolution TEM image (Fig. 1g) implies that the well-defined lattice fringe with an interplanar distance of 3.44 \AA , corresponding the (020) plane of MoO_3 . Moreover, some atomic-level distortion could be clearly observed (remarked by red dots, also see Fig. S6, supporting information), which is due to the presence of oxygen vacancies. The selected area electron diffraction (SAED) pattern was shown in Fig. 1h, indicating the single-crystalline nature of the $v\text{-MoO}_3$ PNB, which is attributed to the (010) zone axis diffraction.

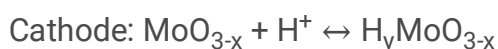
Raman spectroscopy and electron paramagnetic resonance (EPR) spectroscopy were carried out to study the samples. Both the MoO_3 NB and the $v\text{-MoO}_3$ PNB show three sharp Raman bands located at 663 cm^{-1} ($\text{B}_{2g}/\text{B}_{3g}$, *vas*, O-Mo-O stretch), 816 cm^{-1} (A_g , *vas*, Mo=O stretch) and 993 cm^{-1} (A_g , *vas*, Mo=O stretch, Fig. 2a),³⁸ confirming they are orthorhombic structure of $\alpha\text{-MoO}_3$. The $v\text{-MoO}_3$ PNB exhibits a remarkable reduction in Raman peak intensity compared to the MoO_3 NB, implying the successful introduction of oxygen vacancies. Fig. 2b shows the Electron Paramagnetic Resonance (EPR) spectroscopy of MoO_3 NB and $v\text{-MoO}_3$ PNB. The MoO_3 NB almost shows no EPR signal while the $v\text{-MoO}_3$ PNB manifests a remarkable EPR signal in fields of 3250-3750 Gs. The g_1 can be ascribed to the O^- as the paramagnetic center and the g_2 is related to the Mo^{5+} as the paramagnetic center.^{39, 40} The presence of Mo^{5+} further indicates the presence of oxygen vacancy in $v\text{-MoO}_3$ PNB.

X-ray photoelectron spectroscopy (XPS) was conducted to further investigate the surface properties and chemical composition of the samples. The survey spectroscopy shows the sign of Mo, C, and O elements in both MoO_3 NB and $v\text{-MoO}_3$ PNB (Fig. S7, supporting information). Fig. 2c presents the high-resolution XPS spectra of Mo 3d, which can be divided into four peaks, 236.1 eV for $\text{Mo}^{6+} 3d_{3/2}$, 232.9 eV for $\text{Mo}^{6+} 3d_{5/2}$, 235.4 eV for $\text{Mo}^{5+} 3d_{3/2}$, and 232.2 eV for $\text{Mo}^{5+} 3d_{5/2}$, respectively.^{41, 42} The atomic ratio of $\text{Mo}^{5+}/\text{Mo}^{6+}$ can be employed to character the oxygen vacancies of MoO_3 . For MoO_3 NB, the atomic ratio of $\text{Mo}^{5+}/\text{Mo}^{6+}$ is estimated to be 0.13 (corresponding to $\text{MoO}_{2.93}$), while the corresponding value for $v\text{-MoO}_3$ PNB increases to 0.38 (corresponding to $\text{MoO}_{2.82}$), suggesting that the partial reduction of MoO_3 and the oxygen vacancies have been increased after the reduction treatment. The peak of 530.6 eV is observed for both MoO_3 and $v\text{-MoO}_3$ PNB from the O1s core-level XPS spectra (Fig. 2d), which is ascribed to the Mo-O bond. Moreover, the O 1s XPS peak of 531.4 eV for MoO_3 NB indicates the absorption of OH^- on the surface of MoO_3 NB, while for the $v\text{-MoO}_3$ PNB, the peak corresponding to OH^- is missing, and there appear two peaks located at 532.4 and 531.2 eV that can be assigned to the sign of PO_3^- and H_2PO_4^- ,⁴³ further confirming the partial reduction of MoO_3 by phosphate ions during the annealing process.

To evaluate the H⁺ storage capability, cyclic voltammetry (CV) tests were carried out in 1.0 M H₂SO₄ with a standard three-electrode system with Ag/AgCl as reference electrode, Pt wire as counter electrode, and the MoO₃ modified carbon paper (1*1 cm²) as working electrode, respectively. Fig. 3a shows the first three CV curves of v-MoO₃ PNB at a scan rate of 1 mV s⁻¹ at the potential range from -0.5 to 0.3 V. One can observe three pairs of redox peaks of 0.074 V/0.01 V, 0.032 V/-0.04 V, and -0.371 V/-0.384 V that are related to the insertion and deinsertion of H⁺ into the v-MoO₃ PNB electrode. Notably, the peak current of v-MoO₃ PNB is larger than that of MoO₃ NB (Fig. 3b), implying a higher H⁺ storage capacity for v-MoO₃ PNB, which can be rationally attributed to the higher conductivity (Fig. S8, supporting information) and more activity sites derived from large specific surface area (Fig. S9, supporting information). Moreover, the reaction kinetics of H⁺ insertion and deinsertion were further studied by recording the CV curves at different scan rates from 0.5 to 10 mV s⁻¹ (Fig. 3c). The peak currents and the peak separations increase along with the scan rate increases, which is due to the enhanced polarization at high scan rates. The Randles-Sevcik equation was employed to determine the relationship between the peak currents (*i_p*) and scan rate (*v*). The *i_p* linearly increases with the square root of the scan rate (*v*^{1/2}) over the scan rate range, with the excellent linearity close to 1 (Fig. 3d), indicating a diffusion process control of the H⁺ insertion and deinsertion on the v-MoO₃ PNB electrode.

The charge and discharge profiles from 1 A g⁻¹ to 20 A g⁻¹ of the v-MoO₃ PNB are shown in Fig. 4a. Even at an ultra-high current of 20 A g⁻¹, three obvious pairs of charge and discharge plateaus can be observed, which match well with the three-step redox behavior in the CV curves. While the charge and discharge plateaus of MoO₃ NB can't be recognized at large current (Fig. S10, supporting information), implying the high rate capability for the v-MoO₃ PNB thanks to its improved conductivity. Fig. 4b shows the capacity at different current density of the v-MoO₃ PNB, which delivers discharge capacities of approximately 248.2, 245.4, 210.8, and 198.7 mAh g⁻¹ at currents of 1, 5, 10, and 20 A g⁻¹, respectively. The Coulombic efficiency is in the range of 97 - 99% can be obtained when the current is reduced to 1 A g⁻¹. However, the MoO₃ NB exhibits a poor rate performance with low specific capacity and inferior capacity recovery (Fig. S11, supporting information). Fig. 4c shows the stability of the v-MoO₃ PNB for H⁺ insertion and deinsertion. At a current of 10 A g⁻¹, above 92% of its initial capacity can remain with an average Columbia efficiency of 96% after 200 cycles, which is superior to those of MoO₃ NB (Fig. S12, supporting information).

Given its quite good H⁺ storage capability, we developed a alkali-acid Zn-MoO₃ hybrid battery that OH⁻ are involved on alkaline Zn conversion anode while H⁺ insertion/deinsertion takes place in acidic v-MoO₃ PNB cathode (Fig. 5a).



In this as-developed hybrid device, the redox reactions of anode and cathode can proceed in their optimal conditions with potential of harvesting the so-called electrochemical neutralization energy (ENE),^{44, 45, 46, 47, 48} which can significantly enhance the voltage and energy density of energy devices. Fig. 5b shows the CV curves of the Zn anode in alkali and the v-MoO₃ PNB cathode acid at a scan rate of 1 mV s⁻¹. Both electrodes show redox activity at their individual potential windows, which indicates the availability and feasibility for fabricating alkali-acid Zn-MoO₃ hybrid battery. The as-constructed alkali-acid Zn-MoO₃ hybrid battery (Fig. 5b) shows one prominent pair of redox peaks in the potential range of 1.2 V to 1.6 V. As a result, the battery shows a high open-circuit voltage (OCV) of about 1.85 V (Fig. 5c), higher than most of aqueous battery.^{49, 50, 51, 52, 53} And the value is constant for 60 mins, implying the decent stability of the hybrid battery. Moreover, a single battery can power a red light-emitting diode (LED, 1.8-2.2 V, Fig. S13, supporting information), further demonstrating the high voltage of the as-built battery. It is noted that the OCV of the battery varies when the electrolyte is different (Fig. S14, supporting information) because the H⁺ insertion and deinsertion are sensitive to the pH value of electrolytes, including the current and potential (Fig. S15, supporting information).

Fig. 5d shows the charge and discharge profiles from 1 A g⁻¹ to 10 A g⁻¹ of the alkali-acid Zn-MoO₃ hybrid battery. The distinct charge and discharge plateaus can be observed in all curves at various current density. The alkali-acid Zn-MoO₃ hybrid battery can deliver a discharge capacities of 198.2, 170.2, 157.8, and 139.2 mAh g⁻¹ at currents of 1, 2, 5, and 10 A g⁻¹, respectively (Fig. 5e), which implies the battery can afford an excellent rate performance. Moreover, when the current density was back to 1 A g⁻¹, the reversible specific capacity could be recovered, indicating excellent reversibility of the battery even after high rate current. Meanwhile, high Coulombic efficiency in the range of 94 - 98% can be achieved. Fig. 5f exhibits the charge and discharge profiles (GCD) of the alkali-acid Zn-MoO₃ hybrid battery in different cycle number at a current density of 5 A g⁻¹, in which one can clearly observe two pairs of GCD voltage plateaus. The dominant GCD voltage plateaus are located at about 1.45 V and 1.85 V for the first charge-discharge process, and they are positioned at a stable level of about 1.91 V and 1.51 V in the following cycles, indicating that the alkali-acid Zn-MoO₃ hybrid battery shows a good reversibility and cycling stability. Furthermore, long-term cycling performance of the alkali-acid Zn-MoO₃ hybrid battery confirms the excellent stability. As shown in Fig. 5g, above 90% of its initial capacity can be achieved with an average Columbia efficiency of 95% after 200 cycles at a current of 5 A g⁻¹. The phase of the v-MoO₃ PNB has not been changed after long-term stability test, except for peaks from Nafion at 18° and 26.4°, and crystalline carbon paper at about 25° (Fig. S16, Supporting Information). In addition, the morphology and microstructure of the v-MoO₃ PNB also keep almost unchanged, as demonstrated by the SEM images of the material (Fig. S17, Supporting Information). Moreover, the CV curve of Zn anode shifts for high potential, while that of v-MoO₃ PNB cathode shifts to low potential (Fig. S18, Supporting Information), which may be due to the crossover of H⁺ and OH⁻. For this purpose, we monitor the pH value variation of the catholyte and anolyte during cycling. The concentration of H⁺ and OH⁻ decrease along with cycling

(Fig. S19, Supporting Information), which induces the capacity decay of the alkali-acid Zn-MoO₃ hybrid battery.

To investigate the mechanism of the alkali-acid Zn-MoO₃ hybrid battery, the *ex-situ* XRD measurements of v-MoO₃ PNB electrode were performed during the charge and discharge process (Fig. 6). As shown in Fig. 6b, all the XRD patterns during the charge-discharge processes show three predominant peaks of (020), (040) and (060), indicating that no phase transition exists in the processes, which suggests a solid solution reaction during H⁺ ions insertion and deinsertion. Moreover, the peak located at about 18° is assigned to the Nafion. When discharged to 1.0 V, the peak at 12.7° for the (020) planes of the v-MoO₃ PNB shifts to 12.63°, associated with the (002) planes of H_{0.88}MoO₃,¹⁶ implying the H⁺ ions have been inserted into the v-MoO₃ PNB. When charged to 1.7 V and 2.2 V, the peak derived from the (020) planes returns to 12.67° and 12.7°. During the subsequent discharge process, the (020) peak shifts from 12.7° to 12.63°. These observations reveal that the insertion and deinsertion of H⁺ are reversible on the v-MoO₃ PNB.

Discussion

In summary, we have demonstrated a novel alkali-acid Zn-MoO₃ hybrid battery that hydroxide ions (OH⁻) can be consumed/released on the Zn anode in alkali and hydrogen ions (H⁺) can be inserted/deinserted into/from MoO₃ on the cathode in acid. The hybrid battery exhibits a high voltage of 1.85 V and a reversible capacity of 157 mAh g⁻¹ with a near 100% Coulombic efficiency at a high current density of 5 A g⁻¹, which is contributed to the fast kinetics of charge carriers of H⁺ and OH⁻, improved conductivity and active sites induced by high density of oxygen vacancies in v-MoO₃ PNB, and the utilization of electrochemical neutralization energy. The present work may open a new avenue for developing high voltage and high energy density aqueous electrochemical energy devices.

Methods

Preparation of α -MoO₃ nanobelt (MoO₃ NB): Typically, 10 mL of saturated ammonium heptamolybdate tetrahydrate was added in a beaker. 20 mL of 10% HNO₃ solution was dropped into the beaker with the assistance of stirring. The pH of the mixed solution was adjusted to about 1 by 20% HNO₃. Then, the obtained solutions were transferred into a 50 mL Teflon-line autoclave and heated at 180 °C for 40 h. The α -MoO₃ nanobelt was obtained by washing with absolute ethanol and distilled water for several times and then drying at 60 °C.

Preparation of vacancies abundant MoO₃ porous nanobelt (v-MoO₃ PNB): 100 mg of as-prepared MoO₃ was dispersed in 20 mL of 0.1 M FeCl₃ solution, and then stirring for 6 h. The product of MoO₃ nanobelt with a porous structure (MoO₃ PNB) was collected after washing and drying. 50 mg of the as-collected product was placed in a combustion boat, and 5 g NaH₂PO₄·H₂O at the upstream side of the tube

furnace. The v-MoO₃ PNB was obtained by calcining the MoO₃ PNB powder at 250 °C for 1 h in the Ar atmosphere.

Characterization

The morphologies of samples were checked by field-emission scanning electron microscope (FESEM; Hitachi, SU8010, 5 kV) and transmission electron microscope (TEM, FEI, F20, 200 kV). The phase of products was performed on the powder X-ray diffraction (Hitachi, Miniflex600). X-ray photoelectron spectra (XPS) were collected by ESCALAB 250Xi (Thermo Scientific) XPS spectrometer with an Al K α as the excitation source (1486.6 eV). The N₂ adsorption-desorption isotherms were accomplished on a Micromeritics Instrument Corporation sorption analyzer at 77 K (Micromeritics TriStar II 3020), from which we can obtain the information of specific area and pore properties for samples.

Hydrogen ions insertion/deinsertion measurements

The electrochemical measurements were carried out on a CHI 760E electrochemical work station employing a typical three-electrode system in the solution of 1 M H₂SO₄, in which MoO₃ modified carbon paper electrode, Ag/AgCl, and Pt mesh were used as working electrode, the counter electrode, and the reference electrode, respectively. 10 mg of MoO₃ material was dispersed and sonicated in 500 μ L of a solution containing 250 μ L of deionized water, 50 μ L of Nafion (5%, Dupont) and 200 μ L of ethanol, forming the ink. The MoO₃ modified carbon paper electrode was prepared by dropping 100 μ L of ink on the carbon paper (effective area, 1 cm²) with the mass loading of 2 mg cm⁻².

Assembly and tests of alkali-acid Zn-MoO₃ hybrid battery

To assemble alkali-acid Zn-MoO₃ hybrid battery, MoO₃ modified carbon paper electrode was inserted in 2 M H₂SO₄ solution and the Zn plate was immersed in 4 M NaOH. Between which a Nafion 117 membrane was employed to separate the acid-alkali solution, avoiding bulk neutralization. The Nafion membrane was treated by 1 M H₂SO₄, then 3% H₂O₂ at the temperature of 80 °C for 1 h, respectively. Finally, the Nafion membrane was converted to the Na⁺ conductive membrane after the treatment of NaOH at the temperature of 80 °C for 1 h. The membrane was stored in the 1 M NaSO₄ solution. The open-circuit voltage, CV curves, and open-circuit voltage profiles were recorded on the CHI 760E electrochemical working station. GCD tests were conducted on a battery test system (CT2001 A, LAND).

Declarations

Acknowledgments

We would like to thank the National Natural Science Foundation of China (Project No. 21875253) for financial support.

Author contributions

Z. W. conceived the research project and revised the manuscript. P. C. contributed to the sample synthesis, experimental measurements, and manuscript writing. Y. D. also contributed to the modification of the manuscript. Y. L. contributed to the guidance of the diagram. All authors reviewed and commented on the final version of the manuscript.

Competing interests

The authors declare no competing interests.

References

1. Pan, H., *et al.* Reversible aqueous zinc/manganese oxide energy storage from conversion reactions. *Nature Energy* **1**, 16039 (2016).
2. Candelaria, S. L., *et al.* Nanostructured carbon for energy storage and conversion. *Nano Energy* **1**, 195-220 (2012).
3. Zhang, J., *et al.* *Electrochemical technologies for energy storage and conversion*. John Wiley & Sons (2012).
4. He, P., *et al.* Layered VS₂ Nanosheet-Based Aqueous Zn Ion Battery Cathode. *Adv. Energy Mater.* **7**, 1601920 (2017).
5. Song, M., *et al.* Recent Advances in Zn-Ion Batteries. *Adv. Funct. Mater.* **28**, 1802564 (2018).
6. He, X., *et al.* Stabilized Molybdenum Trioxide Nanowires as Novel Ultrahigh-Capacity Cathode for Rechargeable Zinc Ion Battery. *Adv. Sci.* **6**, 1900151 (2019).
7. Wang, X., *et al.* Hydronium-Ion Batteries with Perylenetetracarboxylic Dianhydride Crystals as an Electrode. *Angew. Chem. Int. Ed.* **56**, 2909-2913 (2017).
8. Jiang, H., *et al.* Insights on the Proton Insertion Mechanism in the Electrode of Hexagonal Tungsten Oxide Hydrate. *J. Am. Chem. Soc.* **140**, 11556-11559 (2018).
9. Jiang, H., *et al.* An Aqueous Dual-Ion Battery Cathode of Mn₃O₄ via Reversible Insertion of Nitrate. *Angew. Chem. Int. Ed.* **58**, 5286-5291 (2019).
10. Wu, X., *et al.* Rocking-Chair Ammonium-Ion Battery: A Highly Reversible Aqueous Energy Storage System. *Angew. Chem. Int. Ed.* **56**, 13026-13030 (2017).
11. Chen, Z., *et al.* Hierarchical Nanostructured WO₃ with Biomimetic Proton Channels and Mixed Ionic-Electronic Conductivity for Electrochemical Energy Storage. *Nano Lett.* **15**, 6802-6808 (2015).
12. Zhu, Y. H., *et al.* Hydronium Ion Batteries: A Sustainable Energy Storage Solution. *Angew. Chem. Int. Ed.* **56**, 6378-6380 (2017).

13. Wu, X., *et al.* Reverse dual-ion battery via a ZnCl₂ water-in-salt electrolyte. *J. Am. Chem. Soc.* **141**, 6338-6344 (2019).
14. Zhang, Z., *et al.* Aqueous rechargeable dual-ion battery based on fluoride ion and sodium ion electrochemistry. *J. Mater. Chem. A* **6**, 8244-8250 (2018).
15. Zhang, Y., *et al.* A novel aqueous ammonium dual-ion battery based on organic polymers. *J. Mater. Chem. A* **7**, 11314-11320 (2019).
16. Wang, X., *et al.* Redox Chemistry of Molybdenum Trioxide for Ultrafast Hydrogen-Ion Storage. *Angew. Chem. Int. Ed.* **57**, 11569-11573 (2018).
17. Liu, Y., *et al.* Polypyrrole-coated α -MoO₃ nanobelts with good electrochemical performance as anode materials for aqueous supercapacitors. *J. Mater. Chem. A* **1**, 13582-13587 (2013).
18. Wen, Z., *et al.* Electrochemical Behavior of α -MoO₃ Nanorods as Cathode Materials for Rechargeable Lithium Batteries. *J Nanosci Nanotech* **6**, 2117-2122 (2006).
19. Lou, X. W., *et al.* Hydrothermal synthesis of α -MoO₃ nanorods via acidification of ammonium heptamolybdate tetrahydrate. *Chem. Mater.* **14**, 4781-4789 (2002).
20. Wu, K., *et al.* MoO₃ nanosheet arrays as superior anode materials for Li- and Na-ion batteries. *Nanoscale* **10**, 16040-16049 (2018).
21. Kim, H-S., *et al.* Oxygen vacancies enhance pseudocapacitive charge storage properties of MoO_{3-x}. *Nat. Mater.* **16**, 454 (2017).
22. Li, G-R., Wang Z-L, Zheng F-L, Ou Y-N, Tong Y-X. ZnO@MoO₃ core/shell nanocables: facile electrochemical synthesis and enhanced supercapacitor performances. *J. Mater. Chem.* **21**, 4217-4221 (2011).
23. Jiang, F., *et al.* MoO₃/PANI coaxial heterostructure nanobelts by in situ polymerization for high performance supercapacitors. *Nano Energy* **7**, 72-79 (2014).
24. Zhang, X., *et al.* Investigation of a branchlike MoO₃/polypyrrole hybrid with enhanced electrochemical performance used as an electrode in supercapacitors. *ACS Appl. Mater. Interfaces* **6**, 1125-1130 (2014).
25. Ji, H., *et al.* In Situ Preparation of Sandwich MoO₃/C Hybrid Nanostructures for High-Rate and Ultralong-Life Supercapacitors. *Adv Funct Mater* **25**, 1886-1894 (2015).
26. Yang, J., *et al.* Creating oxygen-vacancies in MoO₃ nanobelts toward high volumetric energy-density asymmetric supercapacitors with long lifespan. *Nano Energy* **58**, 455-465 (2019).
27. Zhang, G., *et al.* α -MoO_{3-x} by plasma etching with improved capacity and stabilized structure for lithium storage. *Nano Energy* **49**, 555-563 (2018).
28. Suo, L., *et al.* "Water-in-Salt" Electrolyte Makes Aqueous Sodium-Ion Battery Safe, Green, and Long-Lasting. *Adv. Energy Mater.* **7**, 1701189 (2017).
29. Charles, D.S., *et al.* Structural water engaged disordered vanadium oxide nanosheets for high capacity aqueous potassium-ion storage. *Nat Commun* **8**, 15520 (2017).

30. Cai, P., *et al.* Reversible Zn-quinone battery with harvesting electrochemical neutralization energy. *J. Power Sources* **428**, 37-43 (2019).
31. Cai, P., *et al.* An Asymmetric-Electrolyte Zn–Air Battery with Ultrahigh Power Density and Energy Density. *ChemElectroChem* **5**, 589-592 (2018).
32. Cai, P., *et al.* Alkaline-Acid Zn-H₂O Fuel Cell for the Simultaneous Generation of Hydrogen and Electricity. *Angew. Chem. Int. Ed.* **57**, 3910-3915 (2018).
33. Cai, P., *et al.* Covalent organic frameworks derived hollow structured N-doped noble carbon for asymmetric-electrolyte Zn-air battery. *Sci. China Chem.* **62**, 385-392 (2019).
34. Zhong, C., *et al.* Decoupling electrolytes towards stable and high-energy rechargeable aqueous zinc–manganese dioxide batteries. *Nature Energy* **5**, 440-449 (2020).
35. Chao, D., *et al.* An Electrolytic Zn–MnO₂ Battery for High-Voltage and Scalable Energy Storage. *Angew. Chem. Int. Ed.* **58**, 7823-7828 (2019).
36. Kumar V, L., *et al.* Redox Active Polyaniline-h-MoO₃ Hollow Nanorods for Improved Pseudocapacitive Performance. *J. Phys. Chem. C* **119**, 9041-9049 (2015).
37. Huang, L., *et al.* Highly conductive and flexible molybdenum oxide nanopaper for high volumetric supercapacitor electrode. *J. Mater. Chem. A* **5**, 2897-2903 (2017).
38. Xiao, X., *et al.* Intercalation of cations into partially reduced molybdenum oxide for high-rate pseudocapacitors. *Energy Storage Materials* **1**, 1-8 (2015).
39. Singh A, *et al.* Temperature induced modifications in shapes and crystal phases of MoO₃ for enhanced photocatalytic degradation of dye waste water pollutants under UV irradiation. *J. Alloys Compd.* **806**, 1368-1376 (2019).
40. Bai, S., *et al.* Ultrasonic synthesis of MoO₃ nanorods and their gas sensing properties. *Sensors and Actuators B: Chemical* **174**, 51-58 (2012).
41. Cui, J., *et al.* Aqueous hydrogenation of levulinic acid to 1, 4-pentanediol over Mo-modified Ru/activated carbon catalyst. *ChemSusChem* **11**, 1316-1320 (2018).
42. Mai L. Q., *et al.* Lithiated MoO₃ nanobelts with greatly improved performance for lithium batteries. *Adv. Mater.* **19**, 3712-3716 (2007).
43. Zhai, T., *et al.* Phosphate ion functionalized Co₃O₄ ultrathin nanosheets with greatly improved surface reactivity for high performance pseudocapacitors. *Adv. Mater.* **29**, 1604167 (2017).
44. Zhang, M., *et al.* Ru-RuO₂/CNT hybrids as high-activity pH-universal electrocatalysts for water splitting within 0.73 V in an asymmetric-electrolyte electrolyzer. *Nano Energy* **61**, 576-583 (2019).
45. Li, Y., *et al.* An electrochemically neutralized energy-assisted low-cost acid-alkaline electrolyzer for energy-saving electrolysis hydrogen generation. *J. Mater. Chem. A* **6**, 4948-4954 (2018).
46. Wang, G., *et al.* Energy-efficient electrolytic hydrogen production assisted by coupling urea oxidation with a pH-gradient concentration cell. *Chem. Commun.* **54**, 2603-2606 (2018).
47. Weng, G., *et al.* Hydrogen battery using neutralization energy. *Nano Energy* **53**, 240-244 (2018).

48. Manzoor Bhat Z., *et al.* Fuel Exhaling Fuel Cell. *J Phys Chem Lett* **9**, 388-392 (2018).
49. Lee B., *et al.* Elucidating the intercalation mechanism of zinc ions into alpha-MnO₂ for rechargeable zinc batteries. *Chem. Commun.* **51**, 9265-9268 (2015).
50. Alfuruqi, MH., *et al.* Electrochemical Zinc Intercalation in Lithium Vanadium Oxide: A High-Capacity Zinc-Ion Battery Cathode. *Chem. Mater.* **29**, 1684-1694 (2017).
51. Li, G., *et al.* Towards polyvalent ion batteries: A zinc-ion battery based on NASICON structured Na₃V₂(PO₄)₃. *Nano Energy* **25**, 211-217 (2016).
52. Kundu, D., *et al.* A high-capacity and long-life aqueous rechargeable zinc battery using a metal oxide intercalation cathode. *Nature Energy* **1**, 16119 (2016).
53. He, P., *et al.* High-Performance Aqueous Zinc-Ion Battery Based on Layered H₂V₃O₈ Nanowire Cathode. *Small* **13**, 1702551 (2017).

Figures

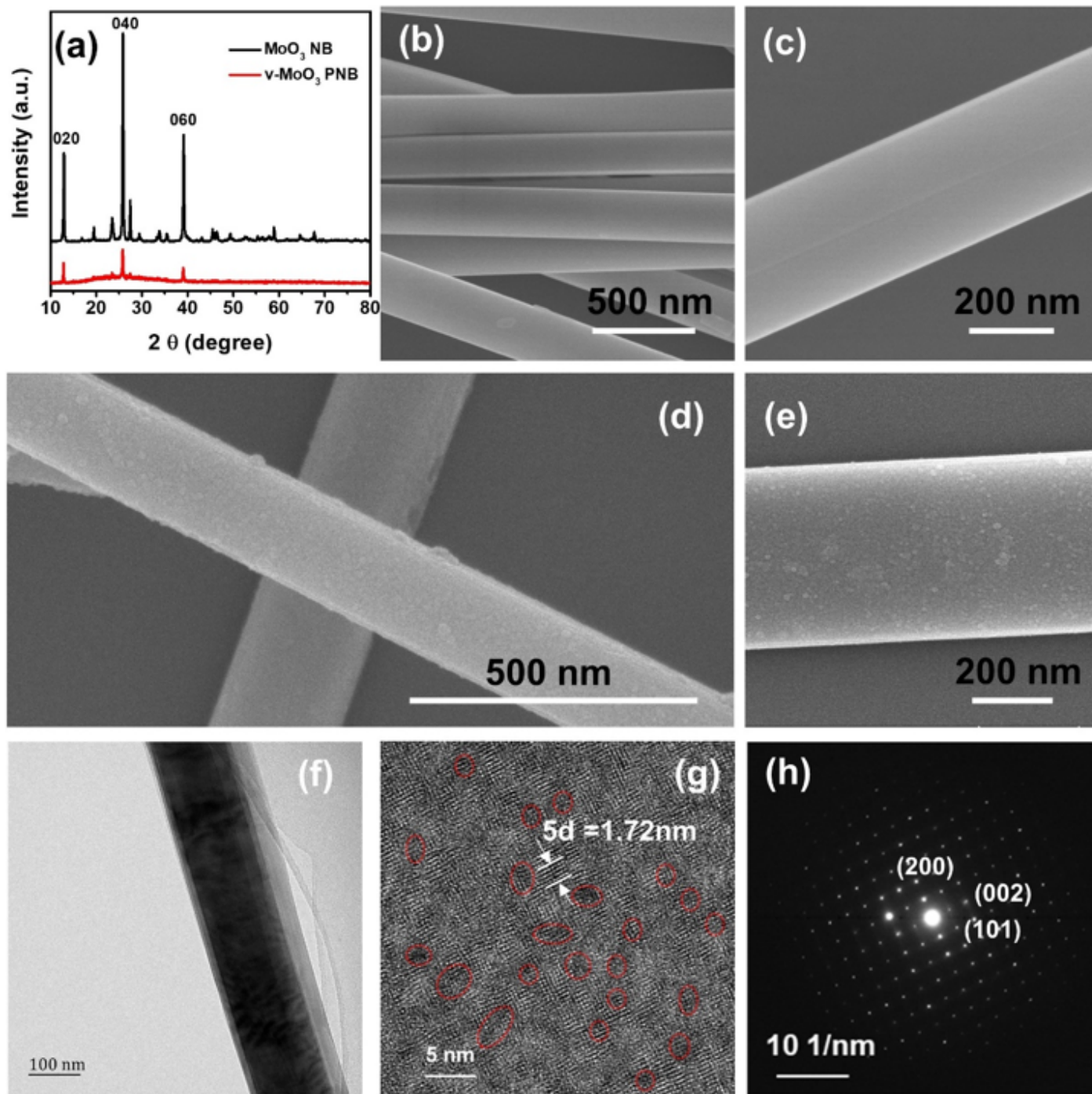


Figure 1

(a) XRD patterns of MoO₃ NB and v-MoO₃ PNB. (b, c) SEM images of MoO₃ NB. (d, e) SEM images; (f) TEM image (g) HRTEM image; and (h) SAED of v-MoO₃ PNB.

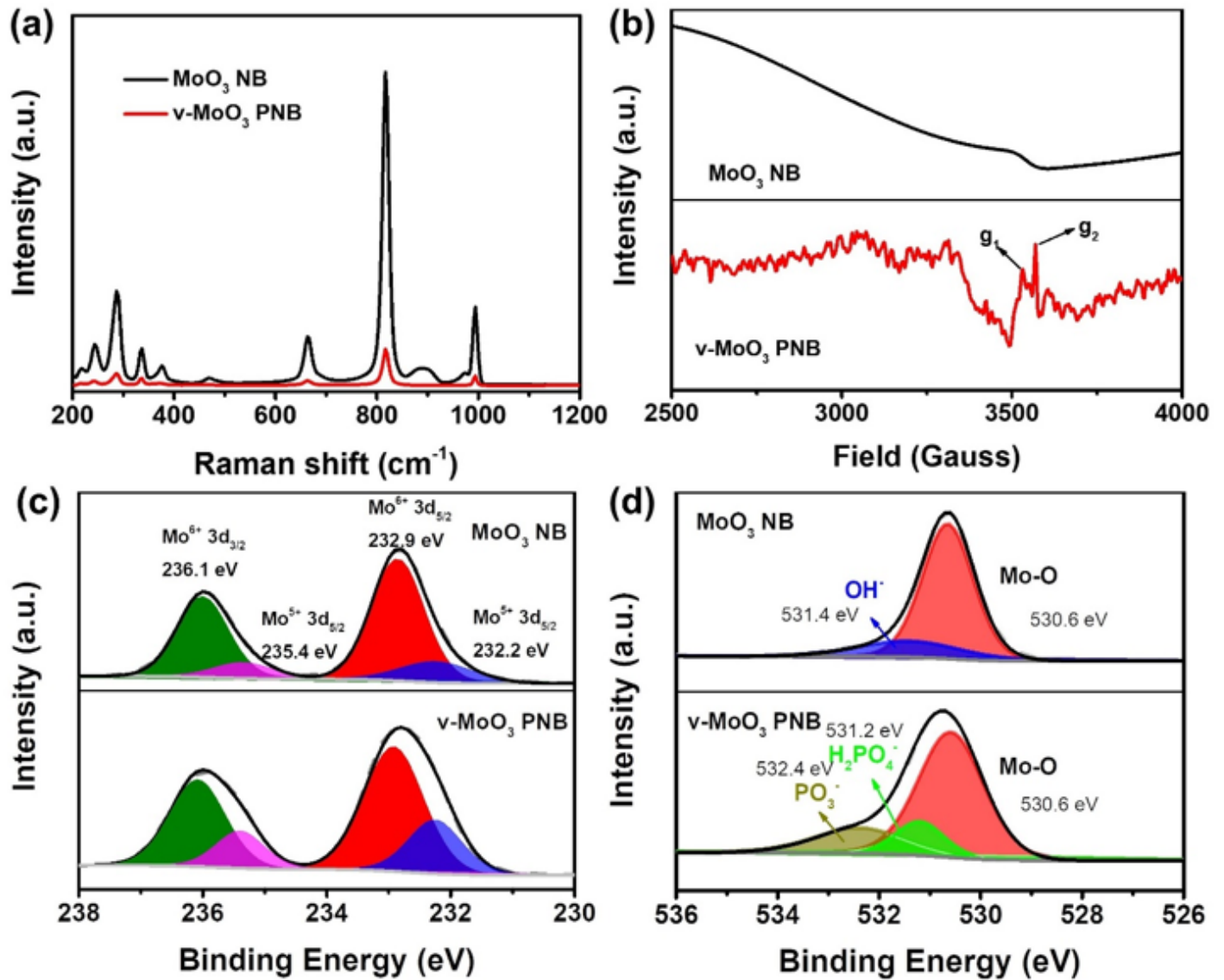


Figure 2

(a) Raman spectra; (b) EPR spectroscopy of MoO₃ NB and v-MoO₃ PNB. (c) Mo 3d core level; (d) O 1s core level of XPS for MoO₃ NB and v-MoO₃ PNB.

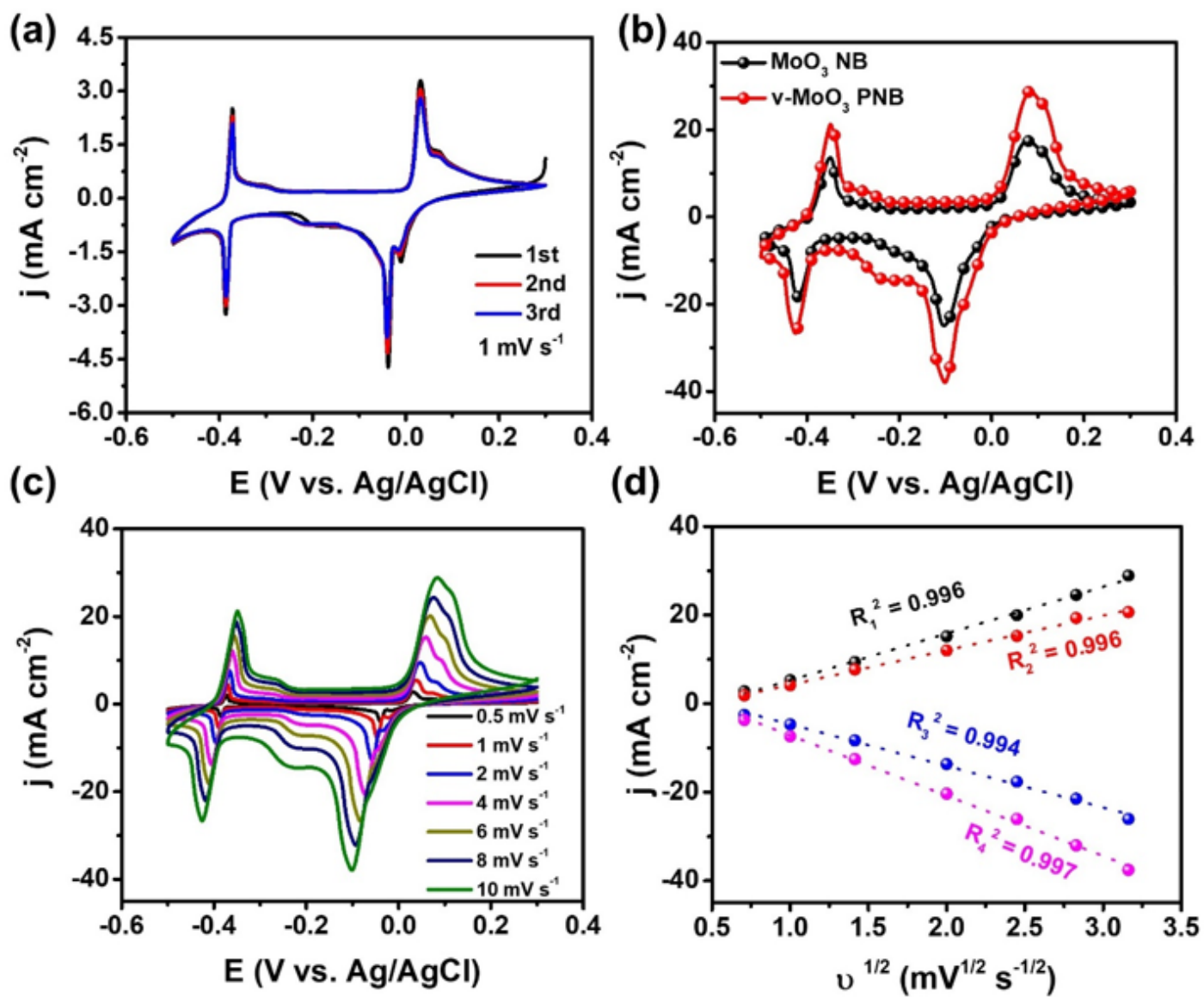


Figure 3

(a) CV curves of the v-MoO₃ PNB electrode for the first three cycles at a scan rate of 1 mV s⁻¹. (b) CV curves of v-MoO₃ PNB and MoO₃ NB electrodes at a scan rate of 10 mV s⁻¹. (c) CV curves of v-MoO₃ PNB at different scan rates from 0.5 to 10 mV s⁻¹. (d) The corresponding plots of peak currents vs. square root of scan rates of v-MoO₃ PNB.

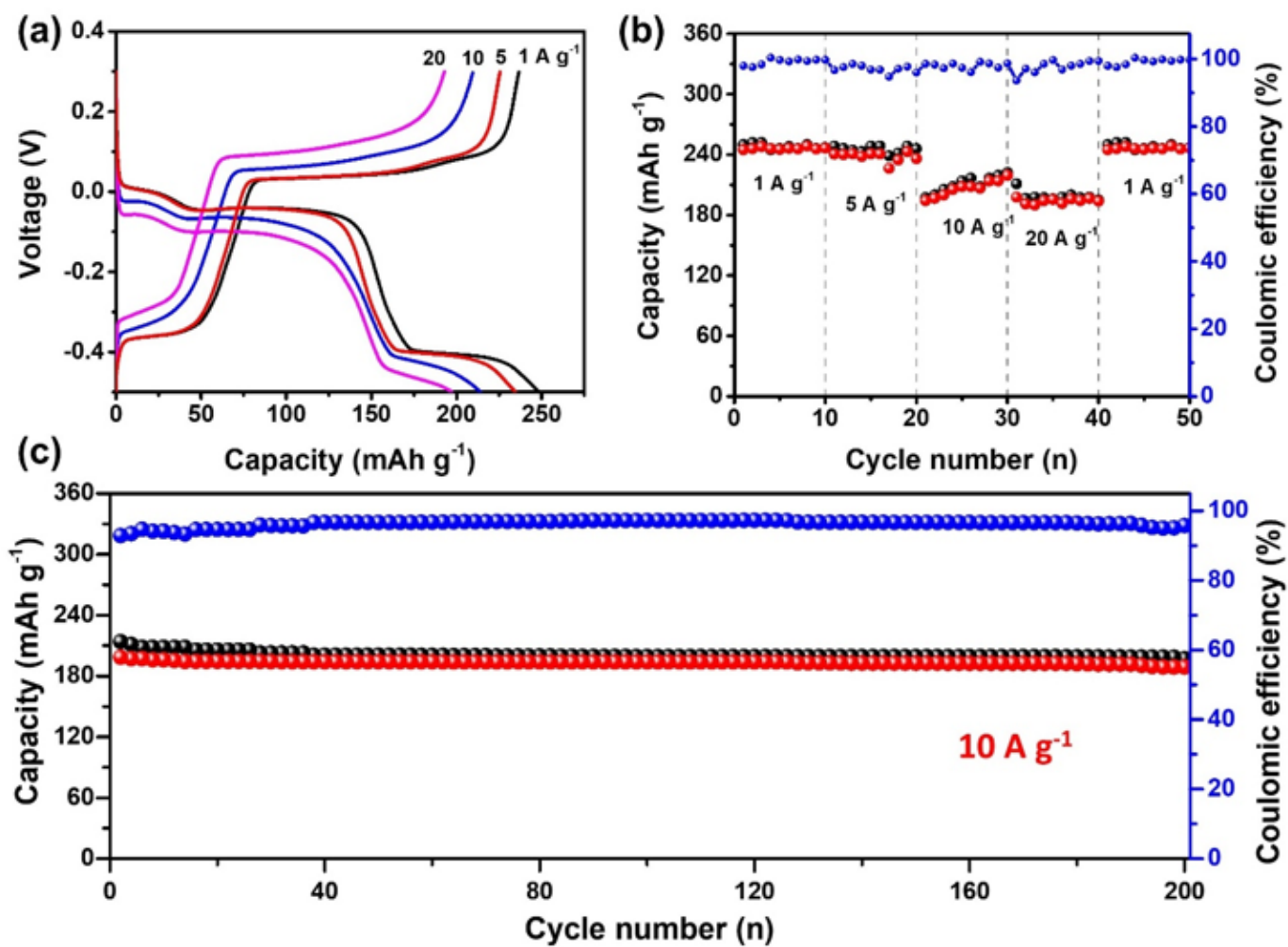


Figure 4

(a) Charge-discharge profiles at different current; (b) Rate performance at current densities from 1 to 20 A g^{-1} ; Cycle performance and Coulombic efficiency at a current density of 10 A g^{-1} of $v\text{-MoO}_3$ PNB electrode.

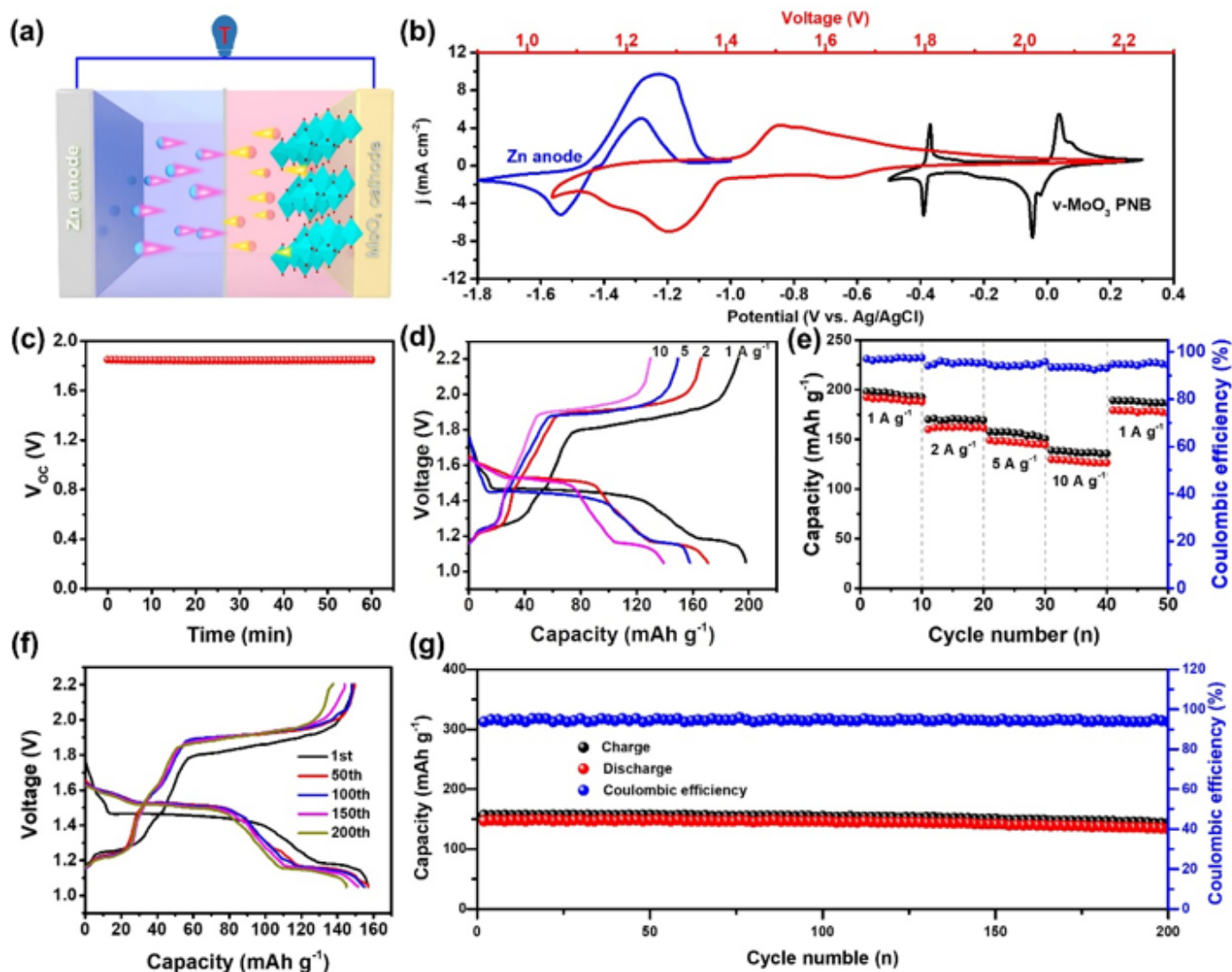


Figure 5

Electrochemical performance of the as-built alkali-acid Zn-MoO₃ hybrid battery. (a) Schematic diagram of the as-built Zn-MoO₃ hybrid battery; (b) CV curves of Zn anode, v-MoO₃ PNB cathode, and the as-built Zn-MoO₃ hybrid battery with a scan rate of 1 mV s⁻¹. (c) Open-circuit voltage (OCV); (d) Charge-discharge profiles at different current; (e) Rate performance at current densities from 1 to 10 A g⁻¹; (f) Charge-discharge profiles at a current density of 5 A g⁻¹ at different cycle number; (g) Long-term cycling performance and corresponding Coulombic efficiency at a current density of 5 A g⁻¹ of the as-proposed Zn-MoO₃ hybrid battery.

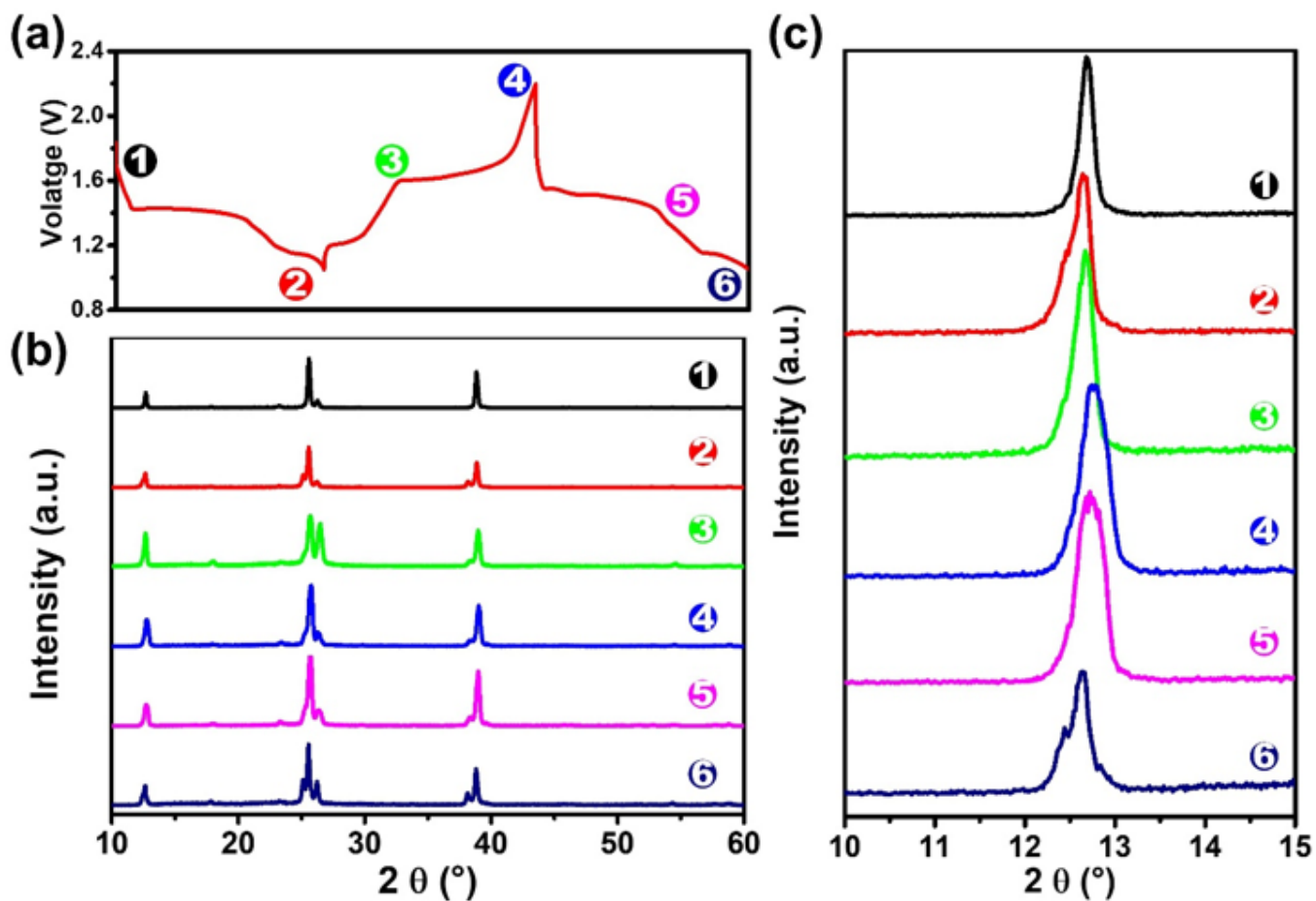


Figure 6

(a) Charge and discharge profiles of the v-MoO₃ PNB electrode in the Zn-MoO₃ hybrid battery. (b) Ex-situ XRD patterns of the v-MoO₃ PNB at different charge-discharge status. (c) Magnified XRD pattern at the range of 10-15°.

Supplementary Files

This is a list of supplementary files associated with this preprint. Click to download.

- [SIZnMoO3battery20200702.docx](#)